Green Chemistry

ROYAL SOCIETY OF CHEMISTRY

PAPER

View Article Online
View Journal | View Issue

Cite this: *Green Chem.*, 2026, **28**, 1566

A crystal-phase-tailored metal heterojunction for dual-site acceleration of alkaline hydrogen evolution

Leyang Song,† Yushuang Gong,† Xiang Liu, Shiling Yuan and An-Liang Wang *

Received 5th November 2025,
Accepted 14th December 2025

DOI: 10.1039/d5gc05906b

rsc.li/greenchem

The electrocatalytic hydrogen evolution reaction (HER) in alkaline media is hindered by sluggish water dissociation kinetics and suboptimal hydrogen adsorption/desorption. Herein, we present a crystal-phase-tailored metal heterojunction, composed of hexagonal close-packed (hcp) Ni and face-centered cubic (fcc) Rh (hcp Ni/fcc Rh), synthesized through a galvanic replacement strategy. Impressively, hcp Ni/fcc Rh exhibits exceptional HER performance, achieving an ultralow overpotential of 20 mV at 10 mA cm^{-2}, which is 2.25 times lower than that of fcc Ni/fcc Rh. Additionally, this catalyst demonstrates long-term stability with a current density of 500 mA cm^{-2} at 1.73 V for over 150 h in an anion exchange membrane water electrolyzer. Mechanistic investigations reveal that the hcp Ni scaffold plays a critical role in enhancing water dissociation by promoting efficient hydrogen generation and facilitating the desorption of *OH to regenerate the Ni sites. Simultaneously, the fcc Rh sites effectively optimize hydrogen adsorption due to the directional interfacial electron transfer from hcp Ni to fcc Rh. This work highlights the potential of crystal phase engineering in advancing heterostructure electrocatalysts for efficient HER.

Green foundation

1. This work introduces a crystal-phase-tailored metal heterostructure (hcp Ni/fcc Rh) that achieves high-efficiency alkaline hydrogen evolution at ultralow overpotential compared to fcc Ni/fcc Rh, advancing sustainable electrocatalysis through rational interfacial and structural design.
2. The obtained catalyst enables 500 mA cm^{-2} at only 1.73 V in an AEM water electrolyzer with over 150 h of stable operation, significantly reducing energy consumption for green hydrogen generation. The galvanic replacement strategy minimizes Rh usage, thereby improving atom economy and resource sustainability.
3. Subsequent research could focus on further reducing Rh loading or substituting it with Earth-abundant analogues while optimizing scalable synthesis routes to decrease precious-metal dependence and enhance overall device efficiency and sustainability.

Introduction

Electrocatalytic water splitting offers a sustainable pathway for green hydrogen production, yet its efficiency is limited by the sluggish kinetics of the HER, especially in alkaline media.[1–5] Under these conditions, the HER proceeds *via* a multistep process involving water dissociation (Volmer step) and subsequent hydrogen evolution (Heyrovsky or Tafel step).[6–10] While Rh-based electrocatalysts possess near-optimal hydrogen binding energy and are considered as promising alternatives to Pt, their performance is fundamentally constrained by two kinetic bottlenecks: (i) inadequate water dissociation capability, and (ii) inefficient management of surface-bound intermediates such as *OH and *H.[11–13] These limitations lead to high energy barriers for water activation, hinder the regeneration of active sites, and restrict surface hydrogen transport, jointly suppressing HER efficiency.

To address these challenges, constructing metal–metal heterostructures has emerged as an effective strategy to regulate interfacial electronic structures and create spatially separated dual active sites for synergistic catalysis.[14,15] By integrating components with complementary functionalities, one promoting water activation and the other facilitating hydrogen desorption, such heterostructures can achieve bifunctional reactivity.[11,16] Nevertheless, most reported systems are limited to isostructural combinations involving conventional crystal phases (*e.g.*, fcc Pd/fcc Rh or fcc Ni/fcc Rh).[17,18] Their exclusive reliance on conventional crystal phases fundamentally constrains the degree of interfacial electron transfer and limits the tunability of dual active sites for simultaneous water dissociation and hydrogen adsorption optimization. Moreover,

---

Key Laboratory for Colloid and Interface Chemistry, Ministry of Education, School of Chemistry and Chemical Engineering, Shandong University, Jinan 250100, Shandong, China. E-mail: alwang@sdu.edu.cn

† These authors contributed equally to this work.

these designs seldom address key mechanistic bottlenecks, such as high *OH desorption energy and substantial *H migration barriers. These barriers impede both active-site regeneration and *H transport, which are critical for efficient HER in alkaline media.[19,20]

In this context, crystal phase engineering, through the deliberate incorporation of an unconventional crystal phase, offers a powerful yet underexplored approach to tailor local coordination environments and electronic structures.[21–23] Such structural modulation can unlock new interfacial catalytic behaviors, which are inaccessible in conventional systems. Nevertheless, integrating disparate crystal phases into a coherent heterojunction remains challenging, primarily due to synthetic challenges in stabilizing unconventional crystal phases within heterojunctions and controlling phase transitions during heterostructure formation. As a result, metal–metal heterostructures comprising dissimilar crystal phases remain largely unexplored, especially for HER applications.

Herein, we report a crystal-phase-tailored metal–metal heterostructure comprising hcp Ni and fcc Rh, constructed *via* a galvanic replacement strategy. The hcp Ni scaffold offers an unconventional coordination geometry that enhances water adsorption and facilitates its dissociation into *H, which readily migrates to adjacent Rh sites. Meanwhile, the generated *OH can be effectively desorbed into the electrolyte, thereby regenerating the Ni active sites. Simultaneously, directional interfacial electron transfer from hcp Ni to fcc Rh optimizes hydrogen adsorption kinetics at Rh sites, accelerating the subsequent desorption steps. As a result, hcp Ni/fcc Rh delivers an ultralow overpotential of 20 mV at 10 mA cm^{-2}, which is 2.25 times lower than that of the fcc Ni/fcc Rh counterpart. When assembled into an anion exchange membrane water electrolyzer (AEMWE), the catalyst achieves 500 mA cm^{-2} at 1.73 V with stable operation sustained over 150 h. This work positions crystal-phase-engineered metal–metal heterojunctions as a powerful paradigm for advanced electrocatalyst design, bridging structural control and interfacial synergy beyond conventional isostructural systems.

Results and discussion

Synthesis and characterization studies

The hcp Ni/fcc Rh heterostructure was synthesized through a two-step method. Initially, hcp Ni nanoparticles with smooth surfaces were prepared *via* a solvothermal method (Fig. S1). Subsequently, a galvanic replacement reaction between hcp Ni nanoparticles and Rh precursors was employed to deposit fcc Rh on the Ni surface, forming the hcp Ni/fcc Rh heterostructure (Fig. 1a; see details in the Experimental section of the SI).

The deposition of Rh is thermodynamically driven by the substantial redox potential difference between Ni^{2+}/Ni (−0.23 V *vs.* reversible hydrogen electrode (RHE)) and Rh^{3+}/Rh (0.76 V *vs.* RHE) couples.[24,25] This potential gap enables a spontaneous galvanic replacement reaction, where Ni undergoes oxidation ($Ni \rightarrow Ni^{2+} + 2e^-$) and Rh^{3+} is concurrently reduced ($Rh^{3+} + 3e^- \rightarrow Rh$). The X-ray diffraction (XRD) pattern reveals characteristic peaks corresponding to hcp Ni (JCPDS No. 45-1027) and fcc Rh (JCPDS No. 05-0685) (Fig. S2), confirming the coexistence of the two phases. The transmission electron microscopy (TEM) image displays nanoparticle morphology with surfaces covered by small, loosely distributed particles (Fig. 1b). The high-resolution TEM (HRTEM) image further reveals distinct lattice fringes with spacings of 0.230 nm for $Ni_{hcp}(010)$, 0.201 nm for $Ni_{hcp}(011)$, and 0.219 nm for $Rh_{fcc}(111)$ (Fig. 1c). A well-defined heterointerface can be observed between the hcp Ni and fcc Rh domains. Fast Fourier transform (FFT) patterns converted from the blue and pink squares in Fig. 1c match well with the simulated electron diffraction patterns of hcp Ni along the [111] zone axis and fcc Rh along the [110] zone axis, respectively (Fig. 1d–g). Elemental mappings confirm a Rh-rich surface (Fig. 1h). To construct an isostructural control sample, an fcc Ni/fcc Rh sample is thermally annealed at 400 °C for 1 h, yielding fcc Ni/fcc Rh with a comparable morphology (Fig. 1i and S3). The HRTEM image of fcc Ni/fcc Rh reveals lattice spacings corresponding to $Ni_{fcc}(111)$ and $Rh_{fcc}(111)$ (Fig. 1j). The corresponding FFT patterns from the blue and pink squares in Fig. 1j align well with the simulated electron diffraction patterns of fcc Ni along the [110] zone axis and fcc Rh along the [110] zone axis, respectively (Fig. 1k–n). This result strongly confirms the formation of

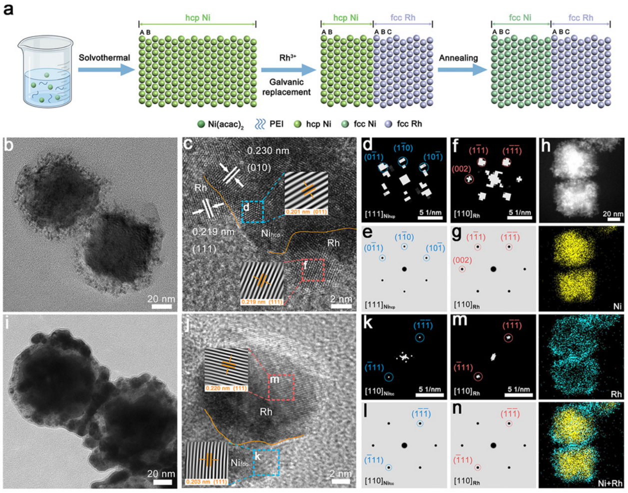

Fig. 1 Scheme and structural characterization. (a) Scheme illustration for the synthesis of hcp Ni/fcc Rh and fcc Ni/fcc Rh. (b) TEM and (c) HRTEM images of hcp Ni/fcc Rh (insets are iFFT images from the blue and pink squares in c). (d) FFT pattern from the blue square in (c). (e) Simulated electron diffraction pattern of hcp Ni along the [111] zone axis. (f) FFT pattern from the pink square in (c). (g) Simulated electron diffraction pattern of fcc Rh along the [110] zone axis. (h) Elemental mappings of hcp Ni/fcc Rh. (i) TEM and (j) HRTEM images of fcc Ni/fcc Rh (insets are iFFT images from the blue and pink squares in j). (k) FFT pattern from the blue square in (j). (l) Simulated electron diffraction pattern of fcc Ni viewed along the [110] zone axis. (m) FFT pattern from the pink square in (j). (n) Simulated electron diffraction pattern of fcc Rh viewed along the [110] zone axis.

heterostructures between fcc Ni and fcc Rh. For comparison, pure fcc Rh with a hollow nanosphere morphology is prepared by selectively etching the Ni component from hcp Ni/fcc Rh in acidic solution (Fig. S4 and S5).

The elemental compositions, chemical states, and electronic interactions were analyzed using X-ray photoelectron spectroscopy (XPS). The full survey spectra confirm the presence of Ni and Rh in both hcp Ni/fcc Rh and fcc Ni/fcc Rh, whereas only Rh signals are observed in fcc Rh (Fig. S6). XPS analysis confirms that metallic Ni and Rh are dominant in all catalysts (Fig. S7–S10). High-resolution Ni 2p spectra of hcp Ni/fcc Rh exhibit three doublets, corresponding to metallic Ni^0 (853.1, 870.3 eV), Ni^{2+} (856.1, 874.0 eV), and satellites (Sat., 861.2, 880.4 eV).[26] The Rh 3d spectra display peaks assigned to metallic Rh^0 (307.5, 312.3 eV) and Rh^{3+} (308.3, 313.3 eV).[27] The presence of oxidized Ni and Rh species is attributed to surface oxidation upon air exposure.[28,29] Notably, a positive shift of 0.7 eV is observed in the Ni^0 $2p_{3/2}$ peak of hcp Ni/fcc Rh (853.1 eV) compared to that of hcp Ni (852.4 eV), indicating electron depletion at the Ni site (Fig. 2a). In contrast, the Rh^0 $3d_{5/2}$ peak in hcp Ni/fcc Rh (307.5 eV) shows a slight negative shift of 0.1 eV relative to that in fcc Rh (307.6 eV), suggesting increased electron density at the Rh site (Fig. 2b). These opposite shifts in binding energy provide compelling evidence of electronic interaction between Ni and Rh, with directional electron transfer from Ni to Rh across the heterointerface.

To elucidate the effect of the Ni crystal phase on the electronic structure and coordination environment of Rh species, X-ray absorption spectroscopy (XAS) was performed. The normalized Rh K-edge X-ray absorption near-edge structure (XANES) spectra show that the absorption edges of both hcp Ni/fcc Rh and fcc Ni/fcc Rh are close to that of Rh foil, but slightly shifted to lower energy (Fig. 2c), indicating the metallic nature of Rh with increased electron density. This electron enrichment is attributed to charge transfer from Ni to Rh, driven by the lower electronegativity of Ni (1.91) relative to Rh (2.28).[30,31] Notably, hcp Ni/fcc Rh displays a more pronounced negative shift compared to fcc Ni/fcc Rh, suggesting a stronger electronic interaction at the heterointerface, induced by the distinct coordination environment provided by the hcp Ni phase. Further insights are provided by the Rh K-edge Fourier-transformed extended X-ray absorption fine structure (FT-EXAFS) spectra. While Rh foil shows a characteristic Rh–Rh peak at 2.47 Å, both hcp Ni/fcc Rh and fcc Ni/fcc Rh exhibit slightly shifted peaks at 2.45 Å (Fig. 2d). The minor bond contraction is attributed to the coexistence of Rh–Ni and Rh–Rh coordination, indicating the formation of heterometallic interactions between Rh and Ni atoms.[32] The least-squares EXAFS fitting curves and corresponding parameters are provided in Fig. S11–S14 and Table S1. The EXAFS oscillation functions of hcp Ni/fcc Rh and fcc Ni/fcc Rh show minor variations in both frequencies and amplitudes, implying a similar local coordination environment for Rh atoms. The Rh K-edge wavelet-transformed EXAFS (WT-EXAFS) analysis of Rh foil shows a local intensity maximum at $k = 9.75$ $Å^{-1}$ and $R = 2.41$ Å, corresponding to the Rh–Rh coordination (Fig. 2e). In contrast, hcp Ni/fcc Rh displays a slightly shifted maximum at $k = 9.80$ $Å^{-1}$ and $R = 2.36$ Å, consistent with the presence of interfacial Rh–Ni bonds. These results further support the existence of phase-dependent electronic modulation at the heterojunction interface.

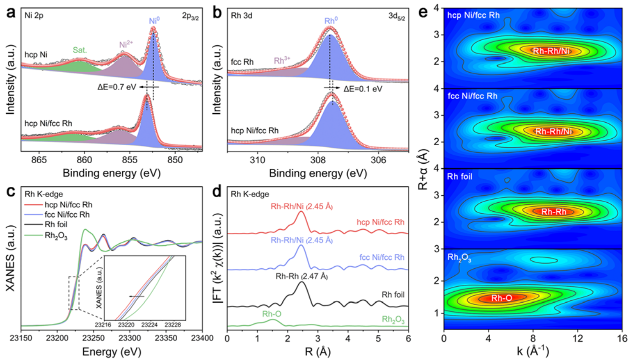

Fig. 2 Chemical state and coordination environment. (a) High-resolution Ni $2p_{3/2}$ XPS spectra of hcp Ni/fcc Rh and hcp Ni. (b) High-resolution Rh $3d_{5/2}$ XPS spectra of hcp Ni/fcc Rh and fcc Rh. (c) Normalized Rh K-edge XANES spectra of hcp Ni/fcc Rh, fcc Ni/fcc Rh, Rh foil, and Rh_2O_3. (d) FT-EXAFS spectra at the Rh K-edge of hcp Ni/fcc Rh, fcc Ni/fcc Rh, Rh foil, and Rh_2O_3. (e) WT-EXAFS contour plots at the Rh K-edge of hcp Ni/fcc Rh, fcc Ni/fcc Rh, Rh foil, and Rh_2O_3.

Electrocatalytic HER performance

The HER performance was evaluated in 1.0 M KOH using a standard three-electrode setup, with the catalyst deposited on carbon paper as the working electrode, a Hg/HgO as the reference electrode, and a graphite rod as the counter electrode. All potentials were calibrated to the RHE scale with *iR* compensation. As shown in Fig. 3a, hcp Ni/fcc Rh exhibits exceptional HER activity, requiring an overpotential of 20 mV to reach a current density of 10 mA cm^{-2}. This value is significantly lower than that of fcc Ni/fcc Rh (45 mV), hcp Ni (210 mV), fcc Rh (59 mV), commercial Pt/C (64 mV) and most reported Rh-based catalysts (Fig. 3g and Table S2). At an overpotential of 100 mV, hcp Ni/fcc Rh delivers a current density of 110 mA cm^{-2}, which is 2.68, 4.78, and 5.24 times higher than that of fcc Ni/fcc Rh (41 mA cm^{-2}), fcc Rh (23 mA cm^{-2}), and Pt/C (21 mA cm^{-2}), respectively (Fig. 3b). The faradaic efficiency (FE) for hydrogen production, measured by the water drainage method, approaches nearly 100% (Fig. S15). It is noteworthy that both hcp Ni/fcc Rh and fcc Ni/fcc Rh significantly outperform monometallic fcc Rh and Pt/C, highlighting the promotional effect of metal–metal heterostructures. Furthermore, hcp Ni/fcc Rh demonstrates superior activity compared to its isostructural counterpart, fcc Ni/fcc Rh, underscoring the pivotal role of crystal phase engineering in optimizing the overall HER performance.

To investigate the influence of Rh content on HER activity, a series of hcp Ni/fcc Rh samples were synthesized by varying the galvanic replacement duration (denoted as hcp Ni/fcc Rh-*t*, where t = 1 h, 3 h, 5 h), and evaluated under identical conditions (Fig. S16, S17 and Table S3). Among these, the sample prepared with galvanic replacement time of 1 h (hcp Ni/fcc Rh-

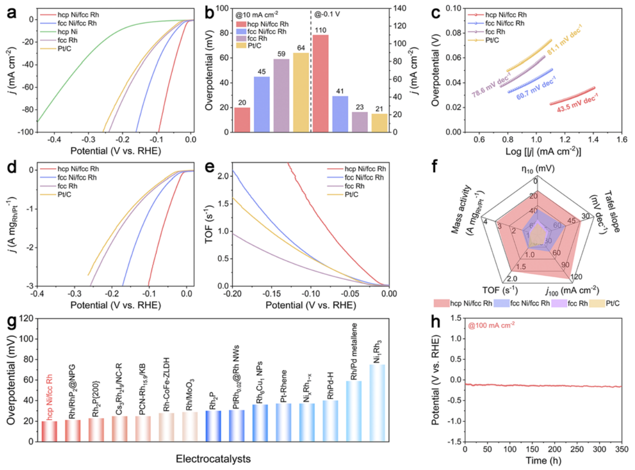

Fig. 3 Electrocatalytic HER performance evaluation. (a) Polarization curves of hcp Ni/fcc Rh, fcc Ni/fcc Rh, hcp Ni, fcc Rh, and Pt/C in 1.0 M KOH. (b) Overpotentials at 10 mA cm^{-2} and current densities at −0.1 V for hcp Ni/fcc Rh, fcc Ni/fcc Rh, fcc Rh, and Pt/C. (c) Tafel plots, (d) polarization curves (current density is normalized to Rh or Pt mass), and (e) TOF of hcp Ni/fcc Rh, fcc Ni/fcc Rh, fcc Rh, and Pt/C. (f) Comprehensive HER metrics comparison (overpotentials at 10 mA cm^{-2}, Tafel slope, current densities, TOF, and mass activity at −0.1 V). (g) Overpotentials at 10 mA cm^{-2} for hcp Ni/fcc Rh and other Rh-based catalysts. (h) Chronopotentiometry curve of hcp Ni/fcc Rh at 100 mA cm^{-2} in 1.0 M KOH.

1 h) exhibits the highest HER activity (Fig. S18–S20). Unless otherwise specified, the term "hcp Ni/fcc Rh" in the following discussion refers specifically to the hcp Ni/fcc Rh-1 h sample.

Comprehensive kinetic analyses were performed to elucidate the origin of the enhanced HER activity of hcp Ni/fcc Rh. The Tafel slope of hcp Ni/fcc Rh is significantly smaller than that of the reference samples, indicating more favorable HER kinetics (Fig. 3c). Electrochemical impedance spectroscopy (EIS) further confirms that hcp Ni/fcc Rh exhibits the lowest charge transfer resistance (R_{ct}), reflecting accelerated charge transfer kinetics (Fig. S21 and S22). To estimate the electrochemically active surface area (ECSA), the double-layer capacitances (C_{dl}) was calculated from cyclic voltammetry (CV) measurements at various scan rates (Fig. S23). A noticeably higher C_{dl} value was obtained for hcp Ni/fcc Rh, indicating a larger number of accessible active sites (Fig. S24). Intrinsic catalytic activity was further evaluated by calculating the mass activity and turnover frequency (TOF). Remarkably, hcp Ni/fcc Rh delivers significantly higher mass activity and TOF values compared to fcc Ni/fcc Rh, fcc Rh, and commercial Pt/C, highlighting its superior intrinsic HER activity (Fig. 3d–f).

Long-term stability is a crucial criterion for HER electrocatalysts. Chronopotentiometry measurements conducted at a current density of 100 mA cm^{-2} reveal negligible potential fluctuations over 350 h, demonstrating excellent stability (Fig. 3h). Post-stability characterization studies further confirms the structural robustness of hcp Ni/fcc Rh, revealing negligible changes in crystal phase, morphology, and surface chemical states (Fig. S25–S27).

Insightful experiments

In the alkaline HER, the kinetics of water dissociation and hydrogen adsorption/desorption on the catalyst surface are key factors governing overall performance.[33,34] To probe the kinetics of water dissociation, hydrogen/deuterium (H/D) kinetic isotope effect (KIE) experiments were conducted.[35] Substituting the KOH/H_2O electrolyte for KOD/D_2O leads to a notable suppression in HER activity for all samples, resulting in KIE values greater than 1.5 (Fig. 4a and b). This strongly indicates that water dissociation acts as the rate-determining step (RDS) in the alkaline HER.[36,37] Strikingly, hcp Ni exhibits significantly lower KIE values compared to fcc Rh, reflecting its superior ability to promote water dissociation (Fig. S28). Upon constructing the hcp Ni/fcc Rh heterostructure, the KIE value decreases substantially, highlighting synergistic enhancement in water dissociation kinetics arising from interfacial electronic interactions. Furthermore, hcp Ni/fcc Rh exhibits a lower KIE value than its fcc Ni/fcc Rh counterpart, underscoring the critical role of the Ni crystal phase (hcp *vs.* fcc) in modulating water dissociation ability. To further assess hydrogen adsorption strength, *tert*-butyl alcohol (TBA) was introduced as a hydrogen radical quencher.[38] As shown in Fig. 4c, the addition of 1.0 M TBA leads to a significant suppression of HER activity for both hcp Ni/fcc Rh and fcc Ni/fcc Rh. Specifically, for hcp Ni/fcc Rh, the overpotentials required to reach current densities of 10 and 50 mA cm^{-2} increase by 66.7% and 53.0%, respectively (Fig. 4d). These increases are substantially larger than those observed for fcc Ni/fcc Rh (43.8% and 27.6%). The more pronounced overpotential elevation upon TBA addition for hcp Ni/fcc Rh indicates a relatively weaker hydrogen adsorption strength, making the adsorbed hydrogen more susceptible to quenching by TBA and thus more likely to suppress HER activity. Therefore, these findings clearly demonstrate that engineering the crystal phase of Ni offers an effective strategy to simultaneously regulate water dissociation kinetics and hydrogen adsorption/desorption strength. This dual-site modulation is critical for optimizing HER performance in alkaline media.

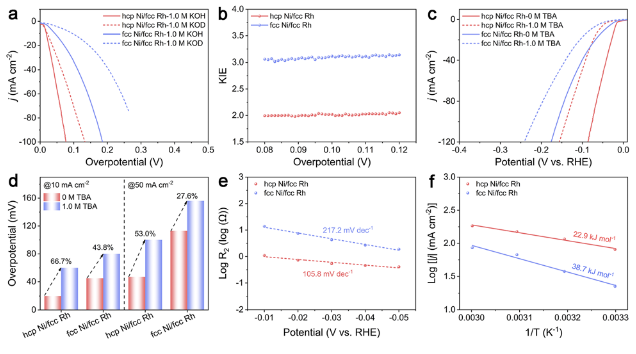

Fig. 4 Experimental insights. (a) Polarization curves of hcp Ni/fcc Rh and fcc Ni/fcc Rh in 1.0 M KOH/H_2O and KOD/D_2O. (b) KIE plots of hcp Ni/fcc Rh and fcc Ni/fcc Rh. (c) Polarization curves and (d) overpotentials at 10 and 50 mA cm^{-2} for hcp Ni/fcc Rh and fcc Ni/fcc Rh in 1.0 M KOH with and without 1.0 M TBA. (e) Plots of log R_2 *versus* potential. (f) Arrhenius plots at −0.05 V.

The superior water dissociation capacity of Ni relative to Rh suggests the occurrence of hydrogen spillover on the hcp Ni/fcc Rh interface. To investigate this phenomenon, operando EIS measurements were conducted under various applied potentials.[39] The resulting Nyquist plots are fitted using a double-parallel equivalent circuit model, in which the second parallel components include hydrogen adsorption capacitance (C_φ) and hydrogen adsorption resistance (R_2) (Fig. S29 and S30).[40] To quantitatively assess hydrogen adsorption kinetics, the potential-dependent R_2 values were analyzed by plotting $\log R_2$ *versus* overpotential to extract the Tafel slopes. As depicted in Fig. S31, hcp Ni/fcc Rh displays a smaller Tafel slope than fcc Rh, suggesting that the incorporation of hcp Ni facilitates hydrogen adsorption and subsequent transfer to Rh sites. Furthermore, the Tafel slope of hcp Ni/fcc Rh is also lower than that of fcc Ni/fcc Rh, further confirming the enhanced hydrogen spillover dynamics enabled by the crystal-phase heterojunction (Fig. 4e). To assess the influence of the Ni crystal phase on overall HER kinetics, the apparent activation energy (E_a) was derived from Arrhenius plots based on current densities measured at a fixed overpotential of 50 mV under varying temperatures (Fig. S32 and S33).[41] Notably, hcp Ni/fcc Rh exhibits a substantially lower E_a of 22.9 kJ mol^{-1} compared to fcc Ni/fcc Rh (38.7 kJ mol^{-1}), further underscoring the vital role of the hcp Ni phase in accelerating HER kinetics (Fig. 4f).

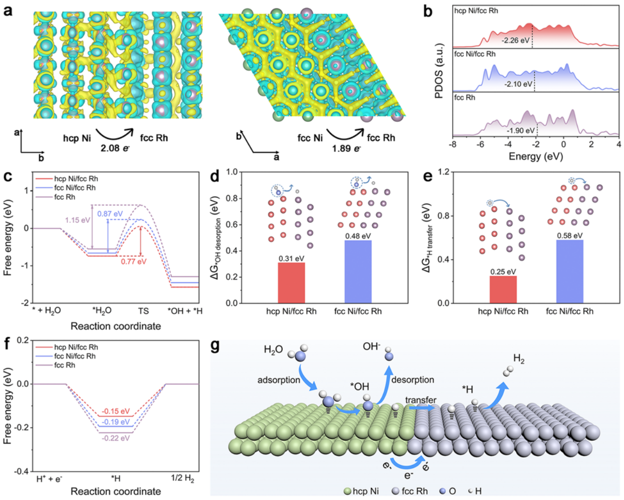

Fig. 5 Theoretical calculations and schematic diagram. (a) Charge density difference maps and Bader charge analysis for hcp Ni/fcc Rh and fcc Ni/fcc Rh. Yellow and cyan clouds represent electron accumulation and consumption, respectively. (b) PDOS profile and corresponding d-band center for hcp Ni/fcc Rh, fcc Ni/fcc Rh, and fcc Rh. The Fermi level is set at zero. (c) Free energy diagrams of water dissociation on hcp Ni/fcc Rh, fcc Ni/fcc Rh, and fcc Rh. (d) Gibbs free energies for *OH desorption ($\Delta G_{*\mathrm{OH\ desorption}}$) on hcp Ni/fcc Rh and fcc Ni/fcc Rh (insets show schematic diagram of *OH desorption). (e) Gibbs free energies for *H transfer ($\Delta G_{*\mathrm{H\ transfer}}$) on hcp Ni/fcc Rh and fcc Ni/fcc Rh (insets show schematic illustrations of *H transfer). (f) Free energies of *H adsorption ($\Delta G_{*\mathrm{H}}$) on hcp Ni/fcc Rh, fcc Ni/fcc Rh, and fcc Rh. (g) Schematic diagram illustrating the HER mechanism on hcp Ni/fcc Rh.

DFT calculations

To elucidate the underlying mechanism of the enhanced HER activity observed for hcp Ni/fcc Rh, density functional theory (DFT) calculations were performed. The optimized heterostructure model was constructed based on the hcp Ni(001) and fcc Rh(111) facets (Fig. S34 and S35). Charge density difference maps and Bader charge analysis reveal interfacial electrons transfer from Ni to Rh. Notably, hcp Ni/fcc Rh exhibits a slightly larger charge transfer (2.08 e^-) compared to fcc Ni/fcc Rh (1.89 e^-) (Fig. 5a), indicating stronger electronic interaction at the hcp Ni/fcc Rh heterointerface. This finding aligns well with the XAS results, further confirming enhanced interfacial charge redistribution at the hcp Ni/fcc Rh heterojunction. Projected density of states (PDOS) profiles show that the d-band center of hcp Ni/fcc Rh is positioned at −2.26 eV, further from the Fermi level compared to fcc Ni/fcc Rh (−2.10 eV) and fcc Rh (−1.90 eV) (Fig. 5b). This downshift in the d-band center suggests weakened adsorption strength of key reaction intermediates (*e.g.*, *H), rationalizing the superior HER kinetics.[42]

As the initial step of the alkaline HER, water adsorption plays a crucial role in determining overall HER performance by governing the kinetics of subsequent Volmer step dissociation.[43] To quantitatively assess adsorption thermodynamics, computational analyses were conducted. The calculated Gibbs free energies for H_2O adsorption ($\Delta G_{*\mathrm{H_2O}}$) indicate that hcp Ni exhibits a more negative value of −0.61 eV compared to fcc Rh (−0.55 eV), suggesting stronger water adsorption on Ni (Fig. S36 and S37). Upon the formation of Ni/Rh heterostructures, $\Delta G_{*\mathrm{H_2O}}$ becomes further reduced, implying that the metal–metal heterostructure facilitates water adsorption. Notably, hcp Ni/fcc Rh shows a significantly lower $\Delta G_{*\mathrm{H_2O}}$ value (−0.74 eV) compared to fcc Ni/fcc Rh (−0.66 eV), highlighting the crucial influence of the Ni crystal phase in enhancing water adsorption (Fig. S38 and S39). To further evaluate water activation kinetics, energy barriers for water dissociation were calculated. As shown in Fig. 5c, the energy barrier on hcp Ni/fcc Rh is 0.77 eV, significantly lower than that on fcc Ni/fcc Rh (0.87 eV) and fcc Rh (1.15 eV) (Fig. S40–S42). This result confirms the accelerated water dissociation kinetics, enabling efficient generation of active *H species. Following water dissociation, the *OH intermediate adsorbed on Ni sites will desorb into the electrolyte. Compared with fcc Ni/fcc Rh (0.48 eV), hcp Ni/fcc Rh exhibits a lower Gibbs free energy for *OH desorption ($\Delta G_{*\mathrm{OH\ desorption}}$, 0.31 eV), indicating facilitated *OH desorption on hcp Ni/fcc Rh, which mitigates poisoning of active sites and enhances active site regeneration (Fig. 5d and S43).[44] Concurrently, the *H intermediate absorbed at Ni sites migrates *via* hydrogen spillover to neighbouring Rh sites. The Gibbs free energy for *H transfer ($\Delta G_{*\mathrm{H\ transfer}}$) is substantially lower for hcp Ni/fcc Rh (0.25 eV) compared to fcc Ni/fcc Rh (0.58 eV), demonstrating more facile hydrogen spillover in the presence of hcp Ni/fcc Rh (Fig. 5e and S44). Additionally, the Gibbs free energy of *H adsorption ($\Delta G_{*\mathrm{H}}$) on hcp Ni/fcc Rh is −0.15 eV, which is closer to zero compared to that on fcc

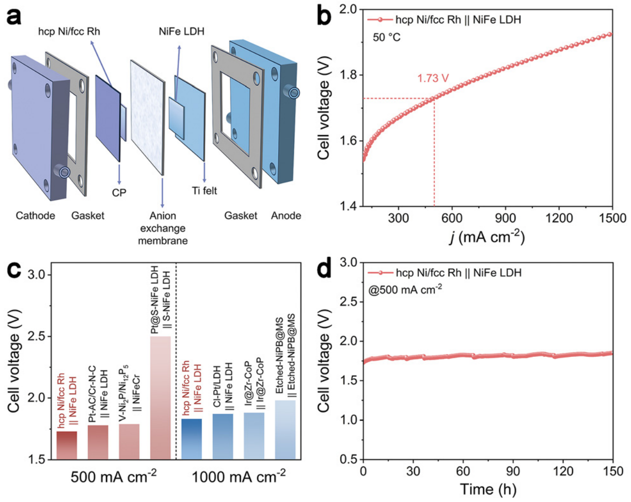

Fig. 6 AEMWE performance evaluation. (a) Schematic diagram of the AEMWE. (b) Polarization (*I*–*V*) curve of the AEMWE measured at 50 °C, using hcp Ni/fcc Rh and NiFe LDH as cathode and anode electrocatalysts, respectively. (c) Comparison of cell voltages at current densities of 500 and 1000 mA cm^{-2} for AEMWE systems employing hcp Ni/fcc Rh and other advanced catalysts. (d) Chronopotentiometry curve at 500 mA cm^{-2} in 1.0 M KOH.

Ni/fcc Rh (−0.19 eV) and fcc Rh (−0.22 eV), indicating more optimal hydrogen absorption/desorption kinetics (Fig. 5f and S45). Collectively, these results unambiguously demonstrate that the incorporation of an unconventional crystal phase in Ni significantly enhances HER catalytic behaviour by simultaneously promoting water dissociation, facilitating hydrogen spillover, and optimizing hydrogen adsorption/desorption, which thereby delivers superior HER performance (Fig. 5g).

AEMWE performance

To evaluate the practical viability of hcp Ni/fcc Rh, an AEMWE was assembled using hcp Ni/fcc Rh supported on carbon paper as the cathode, and NiFe layered double hydroxide (LDH) grown on Ni foam as the anode (Fig. 6a and S46–S50). The electrolyzer was operated in 1.0 M KOH at 50 °C. As shown in the current–voltage (*I*–*V*) curve in Fig. 6b, the AEMWE achieves a high current density of 500 mA cm^{-2} at a low cell voltage of 1.73 V, outperforming most previously reported AEMWE systems employing other advanced catalysts (Fig. 6c and Table S4). Long-term durability was carried out by continuous electrolysis at 500 mA cm^{-2} for 150 h (Fig. 6d). Negligible voltage increase throughout the testing period confirms excellent operational stability. These results highlight the strong potential of hcp Ni/fcc Rh as a high-performance HER catalyst for practical green hydrogen production *via* AEMWE.

Conclusions

We have demonstrated a rational crystal-phase-tailored metal heterostructure strategy to accelerate the alkaline HER by integrating hcp Ni and fcc Rh into a coherent heterojunction *via* a galvanic replacement method. The obtained hcp Ni/fcc Rh heterojunction demonstrates exceptional HER performance, requiring an overpotential of 20 mV at 10 mA cm^{-2}, surpassing fcc Ni/fcc Rh and commercial benchmarks. Combined experimental and theoretical studies reveal that the hcp Ni domains effectively promote water dissociation, while interfacial electron transfer enables fcc Rh to maintain optimal hydrogen adsorption–desorption behaviour. This dual-site synergy reduces the water dissociation energy barrier, facilitates rapid hydrogen spillover and *OH desorption, and promotes efficient hydrogen desorption, thereby markedly accelerating overall HER kinetics. When integrated into an AEMWE, hcp Ni/fcc Rh delivers 500 mA cm^{-2} at a low voltage of 1.73 V, with excellent durability over 150 h of continuous operation. This work highlights the potential of crystal phase engineering in designing advanced heterostructure electrocatalysts through precise interfacial control and synergistic active site modulation.

Author contributions

The manuscript was written through the contributions of all authors. A.-L. W. conceived and supervised the research. L. S. performed most of the experiments and data analysis. X. L. contributed partially to the characterization and testing of the materials. Y. G. and S. Y. performed and analyzed the DFT calculations. A.-L. W. guided the data analysis and revised the manuscript. All authors have given approval to the final version of the manuscript.

Conflicts of interest

There are no conflicts to declare.

Data availability

All data generated or analyzed in this study are included in this manuscript and the supplementary information (SI).

Supplementary information is available. Experimental sections, supplementary Fig. S1–S50, and supplementary Tables S1–S4. See DOI: https://doi.org/10.1039/d5gc05906b.

The datasets used and/or analyzed in this study are available upon request from the corresponding authors.

Acknowledgements

This work was supported by the Qilu Young Scholarship Funding of Shandong University. This work was also supported by the National Natural Science Foundation of China (No. 22005176), the Natural Science Foundation of Shandong Province (ZR2020QE014), the Innovative Team Project of Jinan (No. 202228063), and the Carbon Neutrality Research Institute

Fund (CNIF20230203, CNIF20220206). The authors acknowledge the assistance of Shandong University Structural Constituent and Physical Property Research Facilities/SDU SC&PP Research Facilities/SDU SCPPRF.

References

1 Y. Zhu, X. Wu, Z. Wu, X. Wang, X. Wang, C. Wang, X. Zhu, M. Li, D. Sun, H. Li, Y. Tang and G. Fu, *Adv. Funct. Mater.*, 2024, **34**, 2409324.

2 X. Xiao, Z. Li, Y. Xiong and Y.-W. Yang, *J. Am. Chem. Soc.*, 2023, **145**, 16548–16556.

3 L. Li, P. Wang, Q. Shao and X. Huang, *Chem. Soc. Rev.*, 2020, **49**, 3072–3106.

4 S. Bawari and S. N. Steinmann, *Nat. Energy*, 2025, **10**, 673–674.

5 Y. Du, H. Wang, J. Chen, H. Chen, S. Wang and X. F. Lu, *Chem. Commun.*, 2025, **61**, 17854–17857.

6 N. Danilovic, R. Subbaraman, D. Strmcnik, K.-C. Chang, A. P. Paulikas, V. R. Stamenkovic and N. M. Markovic, *Angew. Chem., Int. Ed.*, 2012, **51**, 12495–12498.

7 J. Zhu, L. Hu, P. Zhao, L. Y. S. Lee and K.-Y. Wong, *Chem. Rev.*, 2020, **120**, 851–918.

8 A. A. Feidenhans'l, Y. N. Regmi, C. Wei, D. Xia, J. Kibsgaard and L. A. King, *Chem. Rev.*, 2024, **124**, 5617–5667.

9 M. N. Hossain, L. Zhang, R. Neagu and S. Sun, *Chem. Soc. Rev.*, 2025, **54**, 3323–3386.

10 Q. Yang, J. Zeng, G. Yang, X. Sun, X. Lin, K. Liu, J. Chen, S. Wang and X. F. Lu, *EES Catal.*, 2025, **3**, 972–993.

11 J. Wu, J. Fan, X. Zhao, Y. Wang, D. Wang, H. Liu, L. Gu, Q. Zhang, L. Zheng, D. J. Singh, X. Cui and W. Zheng, *Angew. Chem., Int. Ed.*, 2022, **61**, e202207512.

12 Y. Guo, X. Tong and N. Yang, *Acc. Mater. Res.*, 2024, **5**, 89–102.

13 Y. Jiang, J. Leng, S. Zhang, T. Zhou, M. Liu, S. Liu, Y. Gao, J. Zhao, L. Yang, L. Li and W. Zhao, *Adv. Sci.*, 2023, **10**, 2302358.

14 Y. Li, L. Li, S. Xu, K. Cui, T. Wang, Z. Jiang and J. Li, *Angew. Chem., Int. Ed.*, 2024, **63**, e202407810.

15 X. Ma, C. Ma, J. Xia, S. Han, H. Zhang, C. He, F. Feng, G. Lin, W. Cao, X. Meng, L. Zhu, X. Zhu, A.-L. Wang, H. Yin and Q. Lu, *J. Am. Chem. Soc.*, 2024, **146**, 20594–20603.

16 M. Lao, K. Rui, G. Zhao, P. Cui, X. Zheng, S. X. Dou and W. Sun, *Angew. Chem., Int. Ed.*, 2019, **58**, 5432–5437.

17 Z. Wang, G. Yang, P. Tian, K. Deng, H. Yu, Y. Xu, X. Li, H. Wang and L. Wang, *J. Mater. Chem. A*, 2023, **11**, 10222–10227.

18 Y. Wang, X. Yu, J. Xu, M. Zhong, J. Hao, M. Gao and X. Lu, *Chem. Eng. J.*, 2025, **505**, 159561.

19 W. Wu, S. Yang, H. Qian, L. Zhang, L. Peng, L. Li, B. Liu and Z. Wei, *Chin. J. Catal.*, 2024, **66**, 1–19.

20 N. Mahmood, Y. Yao, J.-W. Zhang, L. Pan, X. Zhang and J.-J. Zou, *Adv. Sci.*, 2018, **5**, 1700464.

21 J.-W. Zhao, H.-Y. Wang, L. Feng, J.-Z. Zhu, J.-X. Liu and W.-X. Li, *Chem. Rev.*, 2024, **124**, 164–209.

22 X. Zhu, Y.-C. Wang, K. Qu, L. Song, J. Wang, Y. Gong, X. Liu, C.-F. Li, S. Yuan, Q. Lu and A.-L. Wang, *Nat. Commun.*, 2025, **16**, 5742.

23 Y. Du, J. Liu, J. Chen, S. Wang, Y. Tang, A.-L. Wang, G. Fu and X. F. Lu, *Adv. Energy Mater.*, 2025, **15**, 2404113.

24 J. Ran, J. Yu and M. Jaroniec, *Green Chem.*, 2011, **13**, 2708–2713.

25 X. Xia, Y. Wang, A. Ruditskiy and Y. Xia, *Adv. Mater.*, 2013, **25**, 6313–6333.

26 C. Wang, H. Yang, Y. Zhang and Q. Wang, *Angew. Chem., Int. Ed.*, 2019, **58**, 6099–6103.

27 F. Yang, Y. Zhao, Y. Du, Y. Chen, G. Cheng, S. Chen and W. Luo, *Adv. Energy Mater.*, 2018, **8**, 1703489.

28 L. Song, C. Ma, P. Shi, X. Zhu, K. Qu, L. Zhu, Q. Lu and A.-L. Wang, *Green Chem.*, 2024, **26**, 10921–10928.

29 C. He, Y. Yan, Y. Fu, C. Ma, J. Xia, S. Han, H. Zhang, X. Ma, G. Lin, F. Feng, X. Meng, W. Cao, L. Zhu, Z. Li and Q. Lu, *Adv. Mater.*, 2025, **37**, 2418959.

30 D. Jin, A. Yu, Y. Lee, M. H. Kim and C. Lee, *J. Mater. Chem. A*, 2020, **8**, 8629–8637.

31 C. Balamurugan, Y. Y. Kim, Y.-R. Jo, K. Cho, B. Park, W. Kim, N. Lim, Y. Pak, H. Kim, H. Lee, K. H. Chae, J. H. Shim, C. Lee and S. Kwon, *Appl. Catal., B*, 2024, **353**, 124072.

32 W. Zhong, Q.-L. Hong, X. Ai, C. Zhang, F.-M. Li, X.-F. Li and Y. Chen, *Adv. Mater.*, 2024, **36**, 2314351.

33 X. Wang, G. Long, B. Liu, Z. Li, W. Gao, P. Zhang, H. Zhang, X. Zhou, R. Duan, W. Hu and C. Li, *Angew. Chem., Int. Ed.*, 2023, **62**, e202301562.

34 Y. Li, S. Zhang, B. Li, Y. Su, J. Kong and J. Li, *ACS Nano*, 2025, **19**, 7401–7416.

35 Q. Dai, L. Wang, K. Wang, X. Sang, Z. Li, B. Yang, J. Chen, L. Lei, L. Dai and Y. Hou, *Adv. Funct. Mater.*, 2022, **32**, 2109556.

36 Y. Zhang, C. Ma, X. Zhu, K. Qu, P. Shi, L. Song, J. Wang, Q. Lu and A.-L. Wang, *Adv. Energy Mater.*, 2023, **13**, 2301492.

37 W. Li, F. Li, H. Yang, X. Wu, P. Zhang, Y. Shan and L. Sun, *Nat. Commun.*, 2019, **10**, 5074.

38 S. Wang, C. Song, Y. Cai, Y. Li, P. Jiang, H. Li, B. Yu and T. Ma, *Adv. Energy Mater.*, 2023, **13**, 2301136.

39 J. Jiang, G. Xu, B. Gong, J. Zhu, W. Wang, T. Zhao, Y. Feng, Q. Wu, S. Liu and L. Zhang, *Adv. Funct. Mater.*, 2025, **35**, 2412685.

40 H. Fan, Q. Q. Yang, S. R. Fang, Y. N. Xu, Y. Lv, H. Y. Lin, M. Y. Lin, J. K. Liu, Y. X. Wu, H. Y. Yuan, S. Dai, P. F. Liu and H. G. Yang, *Angew. Chem., Int. Ed.*, 2024, **63**, e202412080.

41 J. Huang, H. Sheng, R. D. Ross, J. Han, X. Wang, B. Song and S. Jin, *Nat. Commun.*, 2021, **12**, 3036.

42 K. Zhao, N. Xiang, Y.-Q. Wang, J. Ye, Z. Jin, L. Fu, X. Chang, D. Wang, H. Xiao and B. Xu, *Nat. Energy*, 2025, **10**, 725–736.

43 C. Hu, L. Zhang and J. Gong, *Energy Environ. Sci.*, 2019, **12**, 2620–2645.

44 C. Yang, Y. Gao, Z. Xing, X. Shu, Z. Zhuang, Y. Wang, Y. Zheng, S. Li, C. Cheng, D. Wang and J. Zhang, *Nat. Commun.*, 2025, **16**, 6459.